Micromechanics of fine-grain infiltration in coarse grain sands

Fan Chen, Antoine Wautier, Pierre Philippe, Nadia Benahmed, François Nicot

Noname manuscript No.
(will be inserted by the editor)

Micromechanics of fine grain infiltration in coarse grain sands

Fan Chen* · Antoine Wautier · Pierre Philippe · Nadia Benahmed · François Nicot

Received: date / Accepted: date

Abstract The loss of fine particles can induce mechanical instabilities in granular soils subjected to internal fluid flow. An appealing countermeasure consists of the re-injection of fine grains with the objective of achieving retention in the soil matrix. In this study, both gravity- and fluid-driven infiltration of fine particles into coarse-grain columns with different solid fraction ϕ and size ratios R have been studied using coupled Pore-scale Finite Volume (PFV) and Discrete Element Method (DEM) schemes. Three clogging regimes, surface clogging, deep filtration, and percolation are detected, and the characteristic infiltration depths L_0 are found to grow exponentially with R under gravity- and fluid-driven cases. A probabilistic model derived from pore-constriction size statistics is then put forward, which could efficiently interpret the decaying distribution of fine retention for a given size ratio R and packing density. The mean transit velocity of fine grains follows an increasing trend with R under fixed ϕ and can be collapsed over an almost constant value with the appropriate scaling of $\phi/\sqrt{R}$. Compared to gravitational percolation, more lateral dispersion is found in fluid-driven conditions, and an estimation of the related lateral dispersion coefficient D is provided based on ϕ and R.

Keywords Fine injection ; Suffusion remediation ; DEM-PFV ; Clogging ; Granular material

1 Introduction

Understanding the filtering or clogging of granular materials is of great importance in many industrial domains such as chemical engineering, metallurgical, food, pharmaceutical, and ceramic processing, as well as various geotechnical phenomena like debris flows [17, 18, 26, 39] and bedload sediment transport [14]. Underlying the governing mechanisms of granular material infiltration is rather challenging due to the dynamic collisions of particles in the interstitial void of such porous media. As a result, to date, a reliable description model or controlling technique of granular filtering processes considering both macro- and micro-scale grain behaviors is still missing [15, 17].

Numerous experimental and numerical studies have been conducted to interpret and model the fine sand infiltration in the coarse-grain medium. Three typical regimes of fine grain infiltration behaviors repeatedly

* Corresponding author.

Fan Chen
INRAE, Aix Marseille University, RECOVER, Aix-en-Provence, France.
E-mail: fan.chen@inrae.fr

Antoine Wautier
INRAE, Aix Marseille University, RECOVER, Aix-en-Provence, France.

Pierre Philippe
INRAE, Aix Marseille University, RECOVER, Aix-en-Provence, France.

Nadia Benahmed
INRAE, Aix Marseille University, RECOVER, Aix-en-Provence, France.

François Nicot
Savoie Mont-Blanc University, Laboratoire ISTerre - UMR CNRS 5275, Le Bourget du Lac, France.

occur depending on the size ratio R between coarse and fine particles: (1) instantaneous accumulation or surface clogging when the size ratio is less than about 3, for which only an additional shear-induced segregation mechanism allows for mixing the two material [53, 43]; (2) deep bed infiltration when fine particles are gradually retained, or bridged, at different depths, where grains larger than constriction is unlikely to pass through but clogged inside [21]; (3) spontaneous percolation or unimpeded static infiltration; in this case, fine sands can migrate through the smallest possible voids between large particles without being retained [5, 6, 7, 14]. In practice, undesired free percolation of fine particles can result in degraded quality of mixed granular assemblies, which is also one of the main reasons why a homogeneous distribution of fine and coarse components with a large size ratio can hardly be produced.

In the field of soil mechanics, the well-graded grain size distribution of soil based on stratigraphic analysis may span over several orders of magnitude (such as sand-silt or sand-gravel mixture), which somehow naturally splits the material into fine and coarse components [16, 47]. As a result, fine erosion is likely to occur. As regards soil material strength, research has proved that fine particles play an important role as they affects the peak shearing strength [32, 33], limit the development of plastic strain [37] and improve stability in loose soil matrix [49]. Apart from gravity, various environmental factors also induce unfavorable percolation of soil in nature. One typical geotechnical problem of undesired grain infiltration is suffusion, a process of internal erosion in which soil can lose a part of its finer fraction under the hydraulic action of an internal fluid flow. The long-term suffusion in dikes and embankments can increase the porosity of soil material that may ultimately lead to unexpected damages or failures of structure [44, 4, 30].

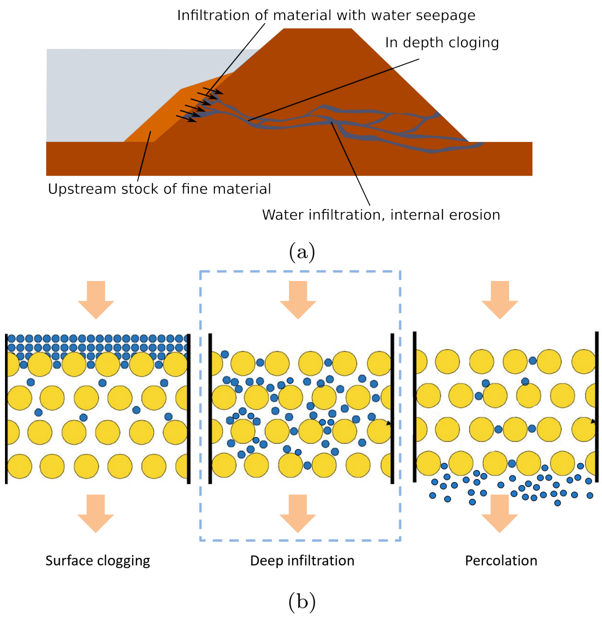

Fig. 1: Schematic of soil remediation method of the eroded dam from upstream fine injection: (a) fine injection method at engineering scale; (b) the three infiltration regimes at the microscopic scale: surface clogging (left), deep infiltration (middle) which is the desired regime for sand remediation, and percolation (right).

Suffusion is linked to fine percolation under the action of an internal flow [46, 36, 3, 10, 11]. As a remediation against suffusion, it is possible to use the flow to infiltrate some fine particles back into the coarse skeleton. However, the size of the fine particles has to be selected in a way to obtain deep infiltration. Such remediation technique is sketched in Figure 1(a), which implements an installed stock of fine material upstream of the eroded dam body. Then, the in-depth infiltration of such fine stock is expected to be induced by the existing fluid flow, during which the injected fine particles would gradually penetrate and finally be retained inside the dam to improve the global soil stability [37, 49]. As mentioned above, it is worth noting that the clogging effectiveness of such material is critical for this remediation concept: the unchanged free sifting of eroded fine grains would simply perpetuate the fine loss process, also injecting too many large grains at once is likely to cause surface clogging as reported by [27, 11], thus would prevent the fine sand from further penetration to repair the erosion part of the dam. Consequently, what this remediation technique aims to achieve is the so-called in-depth clogging, a balance allowing fine sands to penetrate sufficiently into the material while minimizing both free sifting and surface clogging, as depicted respectively in Figure 1(b).

The successful implementation of this remediation attempt requires a comprehensive understanding of infiltration behaviors considering various influencing key factors. Conventionally, filtration could be assessed using the threshold geometrical trapping ratio R_{th}. This trapping ratio is based on the pore structure of mono-dispersed sphere packing - the most restrictive void passage of three large contacting spheres: $R_{th} = d_l/d_{con} = \sqrt{3}/(2-\sqrt{3}) \approx 6.46$, where d_l represent coarse sphere diameter and d_{con} denotes the constriction threshold size that can pass through the void. Existing numerical and experimental studies claimed that the trapping ratio could be slightly larger than R_{th} (around 6.62 to 6.67), due to the occurrence of jammed arches formed by multiple fine grains [41, 20, 29, 34, 35]. Ever since, researchers have focused on either the percolation of fine particles with $R > R_{th}$ or the geometrical trapping threshold for other randomly packed beds [42, 17]. They have analyzed the infiltration behaviors such as percolation velocity, lateral dispersion, and residence time of fine grains falling through the static bed [41, 25, 20, 19, 35]. Since the 1970s, experimental and computational grain infiltration studies have been conducted considering factors such as particle size ratio R, fine particle quantity (collective effect of grain arching), system dimensions, inter-particle restitution coefficient and friction coefficient [12]. Key findings from these investigations include the observation that fine particles tend to maintain a constant infiltration velocity in homogeneous sand columns and exhibit dispersion patterns both perpendicular and parallel to the direction of gravity [17, 35, 25]. In addition, a higher concentration of injected fine particles plays a significant role in enhancing the potential for clogging and impeding the percolation process.

Many previous research simplified the infiltration process by considering mono-dispersed, gravity-driven infiltration when the particle size ratio approaches or is larger than R_{th}, while predominantly disregarding the fluid-driven infiltration into poly-dispersed soil with varied soil packing density, which exists in the case of this remediation method for internal erosion. Therefore, this numerical work, based on the coupled Discrete Element Method (DEM) and Pore-scale finite volume method (PFV), attempts to study both dry and fluid-driven infiltration behaviors of fine sand into granular columns, considering size ratio R from 5 to 12 encompassing the classical geometrical trapping ratio R_{th}. The base soil used in this work adopts the particle size distribution (PSD) of typical Hostun Sand HN1/2.5 mm with dense and loose packing density. The methodology and set-up of the model are introduced in section 2. In section 3, the numerical results like fine retention distribution, averaged infiltration velocity and lateral dispersion are analyzed. By comparing fluid-driven and gravity-driven infiltration, we investigate the effect of lateral flow fluctuations on the infiltration depth thanks to the PFV method that accounts for deviation of fluid paths from the main flow direction. A simple probabilistic model based on pore-constriction size distribution is put forward to interpret the average infiltration distance in terms of traveling lengths through pores and constrictions. This model, despite of its simplicity, has shown encouraging predictive capabilities. Furthermore, an estimation of the lateral dispersion coefficient D can be associated with the mean transit velocity based on ϕ and R.

2 Solid-fluid coupling numerical model

2.1 Discrete element method for the solid phase

The DEM has proved to be a powerful tool for analyzing particle mechanics. Based on simple modeling of contact between interpenetrating rigid particles, the forces and displacements of particles are calculated from Newton's second law [13]. Here, the inter-particle collision behaviors adopt the standard elasto-frictional contact law implemented in YadeDEM, an open-source software [8]. The inter-granular normal and tangential contact forces, F_n and F_t, and the overlaps, $\mathit{\Delta} u_n$ and $\mathit{\Delta} u_t$, are governed by a simple linear elasto-frictional model:

$$\begin{cases} k_n = E\dfrac{2r_1r_2}{r_1+r_2} \\ k_t = \nu k_n \\ F_n = k_n \mathit{\Delta} u_n \\ F_t = \min(k_t \mathit{\Delta} u_t,\ F_n \tan(\mathit{\Phi})) \end{cases} \tag{1}$$

These equations prescribe linear elastic behavior in both the normal and tangential directions with a Coulomb friction limit for the tangential force. In Equation 1, the contact stiffness k_n and k_t are derived from a material modulus E, the radii of the two contacting spheres r_1 and r_2, and the stiffness ratio ν. The friction angle $\mathit{\Phi}$ dictates the maximum allowable tangential force, emulating the sliding relative motions between particles. The DEM parameters are given in Table 1 based on [22, 50].

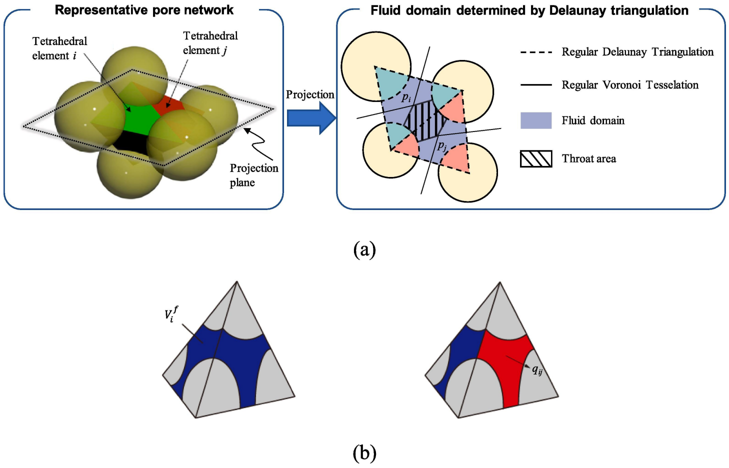

Fig. 2: Delaunay triangulation of the pore network adopted from [18]: (a) schematics of the representative pore network; (b) flux through the tetrahedral element i.

Table 1: Mechanical parameters in the elasto-frictional contact law.

Parameters	Value	Unit
Friction angle (ϕ)	0	$^\circ$
Density (ρ)	2300	kg/m^3
Young modulus (E)	356	MPa
Stiffness ratio (ν)	0.42	-
Friction grain-walls	0	$^\circ$
Coefficient of restitution	0.3	-

2.2 Pore-scale finite volume method for the fluid phase

The PFV method enables simulation of the interconnected fluid flow network in pore bodies of granular matter based on Delaunay triangulation to discretize the pore space [9]. The method facilitates solving the viscous fluid equations at the pore scale via the finite-volume method, as illustrated in Figure 2. It incorporates the fluid's incompressibility and the no-slip boundary condition at the particle-fluid interface. Here, the fluid density (ρ_w) is set as 1000 kg / m^3 while the dynamic viscosity (μ) is equal to 10^{-3} Pa·s. The mass conservation equation for each tetrahedral element i can be expressed as:

$$\dot{V}_{f_i} = -\sum_{j=1}^{4} q_{ij} \tag{2}$$

As Stokes regime predicts a linear relationship between fluid velocity and pressure gradient, the pore fluid flux between two adjacent pores is defined in the Darcy (or Poiseuille) form [9]. By assuming the fluid pressure to be constant in each pore, fluid flux can be computed as:

$$q_{ij} = g_{ij}\frac{p_i - p_j}{\ell_{ij}} \tag{3}$$

where g_{ij} represents the hydraulic conductivity of the constriction that connects pore i to pore j, and ℓ_{ij} denotes the inter-pore distance. It is worth noting that the definitions of these crucial geometrical parameters are not explicitly provided in Equation 3. The precision and reliability of the PFV model depend critically on the careful characterization of these two parameters, which should ideally be based on the specific local geometry of the constrictions linking adjacent pores. For a comprehensive and rigorous elucidation of the definitions of g_{ij} and ℓ_{ij}, as well as a comprehensive validation of the PFV scheme in comparisons with fully resolved CFD simulations, it is recommended to refer to the work in [9].

2.3 DEM-PFV full coupling

Given the fluid velocity field, the force of the fluid on the particle is deduced by integrating the shear and normal stresses acting on the grain surfaces. Eventually, these additional forces can be used in DEM to update the grain positions and the pore space geometry. The solid-fluid interaction force exerted on particle k is expressed as:

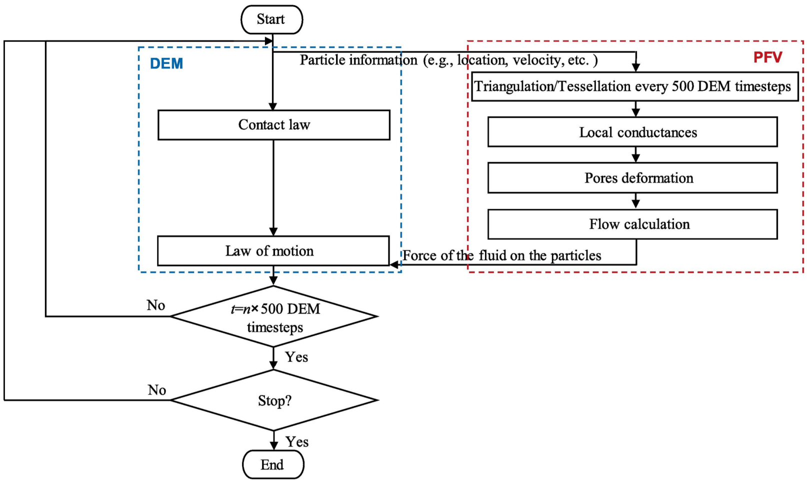

Fig. 3: Flowchart of coupled DEM-PFV method (adopted from [18]).

$$\vec{F}_k = \int_{\partial\Gamma_k} (p_a\vec{n}_k + \tau_{ij}\vec{n}_k)\, ds \tag{4}$$

where p_a is the absolute pressure, τ_{ij} the viscous stress tensor, $\partial\Gamma_k$ the external surface of particle k, and $\vec{n}_k$ the exiting normal unit vector. Calculating the viscous shear force acting on the solid phase denoted as F_{ij}^V, involves integrating the momentum conservation equation over the volume of the throat that connects the two pores. This throat is defined as the space between the centers of the two pores and encompasses the centers of the three particles located between them. This integration results in three distinct terms: the viscous stress applied to the solid phase, the viscous stress within the fluid part, and the sum of the pressures between the two pores. The latter term can be neglected assuming that the pressure gradients are primarily balanced by the viscous stress on the solid phase. As a result, the viscous shear force exerted on the particle is directly proportional to the product of the throat's cross-sectional area, denoted as A_{ij}, and the pressure difference between the two pores.

$$\vec{F}_{ij}^V = \int_{\partial\Gamma_k} \tau_{ij}\vec{n}_k ds \approx A_{ij}\,(p_j - p_i)\,\vec{n}_{ij} \tag{5}$$

In this work, we do not seek to further develop PFV-DEM, but use this algorithm already implemented in YADE to study the mechanisms of infiltration and clogging of fine grains into coarse skeleton [9, 8]. Under the simplified framework, the fluid-solid interaction problem can be solved efficiently by inverting the sparse matrix with specific algorithms [9]. To enhance computational efficiency, updates to the pore network are carried out either when a cumulative deformation threshold is reached or after a predetermined number of time steps. To maintain numerical stability, the time step in DEM is chosen as the minimum value between the critical time step determined by the highest characteristic frequency of the particle system and the critical time step determined by treating the fluid as a viscous damper. As suggested by [51], the updating of the pore network is scheduled at intervals of 500 DEM time steps.

2.4 Model preparation and simulation schemes

This study generates a series of parallelepipedic columns of packed spheres to study the gravity- and flow-driven infiltration behaviors. Two key controlling parameters are considered: the initial packing fraction ϕ for the coarse particles and the size ratio R between mobile fine particles and static coarse spheres. The spheres of the packing replicate the particle size distribution (PSD) of Hostun sand HN1/2.5 mm as given in Figure 4(a). The selection of this PSD introduces a polydispersed base soil, closer to real-world conditions of natural variability in particle sizes than somehow unrealistic mono-size distribution. This narrowly graded PSD is particularly suitable for representing the coarse fraction of soils often subjected to suffusion.

The D_{50} of Hostun sand, referring to the particle size at which 50% of the soil sample's total mass are finer, is equal to 1.71mm and is selected to define fine/coarse size ratio R. Note that various existing filtering criteria [28, 29, 23, 45] are alternatively based on the characteristic value D_{15} as a representative filter pore size, which is here 1.37 mm. Thus, the corresponding ratio of $R_{15} = D_{15}/d$ varies from 4 to 9.6 as $R = D_{50}/d$ increases from 5 to 12. In the following, D_{50} is assumed to satisfactorily account for the geometric properties of the sphere bed. Therefore, it will be used as the characteristic normalizing length within the porous medium appearing in any distance or velocity terms.

The parallelepipedic column has an equal dimension of 40 mm (around $23.5D_{50}$) in width and length, large enough to eliminate the boundary effect resulting in an abrupt increase of void space near the wall [1]. Columns with loose or dense packing density are generated using the gravity-deposition method by tuning the inter-granular friction angle as explained in [2]. The increase in friction promotes a higher global void ratio e of the deposited DEM sample, as shown in Figure 4b. Here, $0°$ and $30°$ are adopted as ideal friction angles to reproduce the densest ($e = e_{min} = 0.61$) and the loosest ($e = e_{max} = 0.85$) sand column as observed experimentally in [40]. The corresponding packings are shown in Figure 4(c) and Figure 4(d) with a solid fraction ϕ equal to 0.62 and 0.54 respectively. Once the two sand columns are deposited and stabilized, the spheres composing this column are fixed to avoid any geometric change in the pore space. Note that the assumption of fixed coarse particles is only valid for small enough hydraulic gradients. This simplification can help accelerate the collision detection procedure in the DEM algorithm. Consequently, the full DEM-PFV coupling applies only to the fine grains.

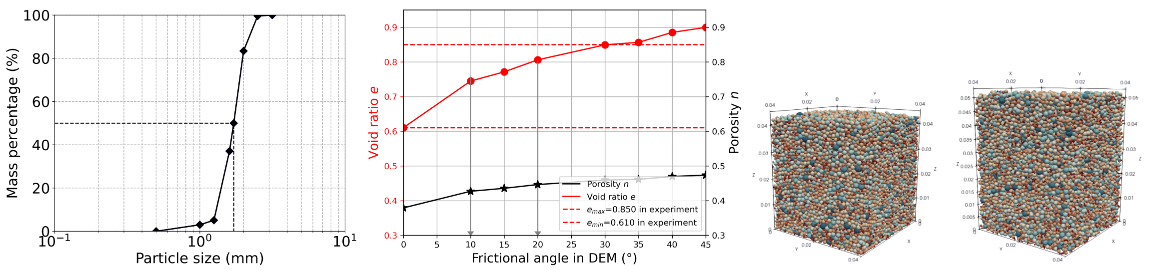

(a) (b) (c) (d)

Fig. 4: Coarse sand column preparation process: (a) adopted PSD of Hostun sand HN1/2.5 mm; (b) void ratio e of gravity-deposited DEM sample with various initial friction angle; (c) densest and (d) loosest sand columns with friction angle of $0°$ and $30°$.

The numerical protocol is based on the repetition of four similar simulations. For each 100 fine particles of the same size, initially positioned randomly in the central area above the column to avoid infiltrating close to the walls, are released either under gravity or imposed hydraulic force (Figure 5(a)). This protocol enables to have statistics over the independently released 400 grains so that no collective effects exist within the simultaneous release of 100 grains.

Eight different fine sizes are considered, with the sizes ratio $R = D_{50}/d$ varying from 5 to 12. The inter-particle friction coefficient is set to 0 during the infiltration process. The coefficient of restitution is set to 0.3 as suggested in [2]. The gravity in dry infiltration cases is enlarged to 1000 times to reduce computational cost. This simulation scheme systematically includes two different packing densities of the sand columns, gravitational or fluid-driven infiltration, and eight varied ratios R. In the fluid-driven infiltration case, the granular filters were exposed to a hydraulic gradient of 5 imposed in the same direction as gravity. To isolate the effect of hydrodynamic forces on fine movement in fluid filtration processes, gravity was set to zero (Figure 5). In the coupled DEM-PFV, the calculation of hydraulic forces acting on individual particles is performed at each time step, taking into account the characteristics of the pore network. All the simulations are stopped either when all fine particles have either been trapped or reached the bottom of the column.

3 Numerical simulation results

3.1 Fine retention distribution

The retention of fine particles trapped during their transit through the porous column is firstly illustrated. In Figure 6, the column is sub-divided by equal-distance layers for both loose and dense columns, and the percentages of clogged fine sands in each layer are represented as shown by the histograms (blue for the dense column and red for the loose column). The dry and fluid-driven cases with R equals 5, 7, 8, 10, 11, and 12 are plotted in the first and second rows of Figure 6, respectively.

Here, surface clogging is observed with R smaller than 7 (R_{15} smaller than 5.6) as over 95% of the fine sands are trapped within a shallow depth of less than $10D_{50}$ in dense or loose columns. Next, as R increases from 8 to 10 (R_{15} from 6.4 to 8.0), deep infiltration occurs with a major fraction of fine sands

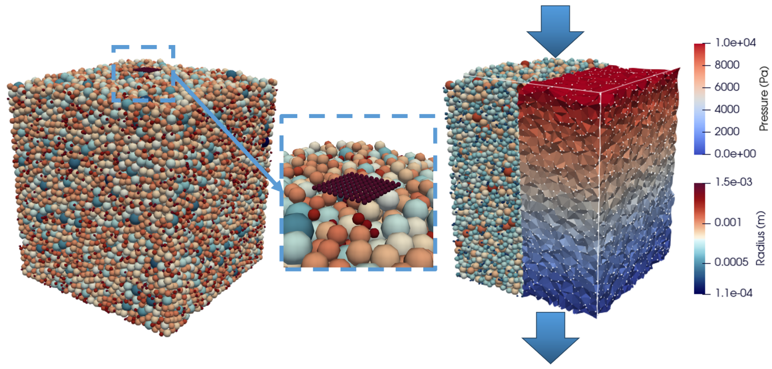

(a) (b)

Fig. 5: Initiation of fine infiltration simulation: (a) fine grains positioned above the coarse-granular column; (b) fluid-driven infiltration by coupled DEM-PFV.

retained inside the sand column as their infiltration is facilitated by the disappearance of surface clogging. Specifically, the fine sands are more uniformly distributed in the dense column when R=10, whereas in the loose column, fine grains tend to accumulate at the bottom layer. When R exceeds 10 (R_{15} exceeds 8.0), a clear percolation of fine grains is observed in both dense and loose columns, and most fine grains finally travel through the whole column. These results are consistent with existing research on the size effect of particle segregation [17, 53, 43]. On the other hand, dry or fluid-driven infiltration seems to obtain a similar result concerning the fine distribution (Figure 6), which requires detailed quantitative comparison.

Compared to the loose column, the dense case shows a shift in the R values at the transition between successive regimes. This can be explained by considering pore-constriction size statistics. Figure 7 provides the probability distribution function (PDF) of pores and constrictions in loose and dense columns based on Delaunay triangulation implemented in the PFV method. A constriction is defined as the smallest cylindrical channel connecting each pair of neighboring pores. It is noted that no merging criteria are used here to determine pores when joint tetrahedrons are too elongated [48]. It can be seen that the dense column has clearly narrowly distributed pore and constriction sizes compared to the loose base soil whose corresponding ranges are much larger. The reduction of pore-constriction space in dense soil samples promotes clogging of fine grains thus inhibiting the infiltration. These physical-based statistics lead to a simple model in the following sections to interpret the fine retention results.

3.2 Characteristic infiltration depth

Based on Figure 6, the gradual process of sieving can be shown in Figure 8 using the so-called passing fraction, i.e., the percentage of fine sands able to reach a given depth along the column. The data from the last layer is disregarded in the fitting process to avoid boundary effects. Similarly, it is observed that the fine sands are filtered within a short distance with a small R. As R increases, fine sands become progressively clogged during infiltration. From Figure 8, the curves in the loose column move to the upper right compared to dense cases, showing an enhanced penetration depth.

Previous research proposed an exponential decaying function to determine this phenomenon in homogeneous soil sample [18]. Therefore, a global exponential fitting curve is adopted for the distribution of fine sands retention $P(z) = P_0 e^{-z/L_0}$, where z is the penetration depth and P_0 as the initial value of fine sands retention and L_0 the characteristic infiltration depth (trapping coefficient in some filtration studies). It is noted that for the probability density function (PDF) $P_0 = 1/L_0$ by normalization (integral of P from 0 to infinity is 1). L_0 is the key parameter to determine the decaying characteristics of fine sands retention. The exponential curves fit satisfactorily with the passing fraction data as shown in Figure 8. It is worth noting that L_0 also coincides with the mean penetration depth since:

$$L_{\text{avg}} = \int_0^\infty \frac{z}{L_0} e^{-z/L_0}\, dz = L_0 \tag{6}$$

L_0 values are plotted in Figure 9 against the size ratio R under different infiltration conditions. The analysis reveals an exponential growth pattern of L_0 with R for both loose and dense columns. Specifically, the mean traveling distance of fine grains in the loose column is two or three times greater than in the dense one. This finding demonstrates the influence of packing density on fine infiltration. However, the difference between loose and dense columns is almost negligible at the beginning of the curves for R smaller than

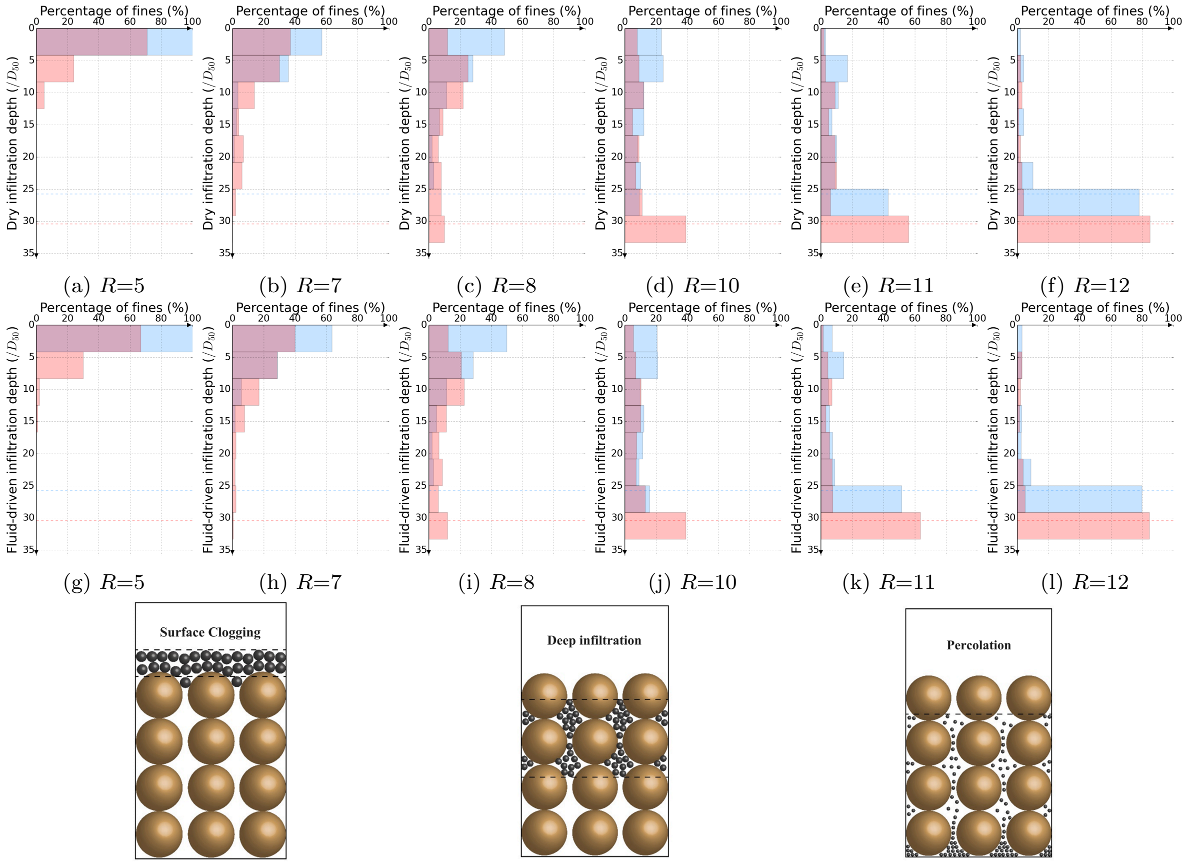

(a) R=5 (b) R=7 (c) R=8 (d) R=10 (e) R=11 (f) R=12

(g) R=5 (h) R=7 (i) R=8 (j) R=10 (k) R=11 (l) R=12

(m) (n) (o)

Fig. 6: Spatial distribution of retained fine sands with size ratios of R=5, 7, 8, 10, 11 and 12: blue and red histograms represent results from the dense and loose sand column; first rows ((a) to (f)) is dry infiltration and the second row ((g) to (i)) is fluid-driven infiltration; schematics of the three infiltration regimes encountered: surface clogging (m); deep filtration (n); percolation (o).

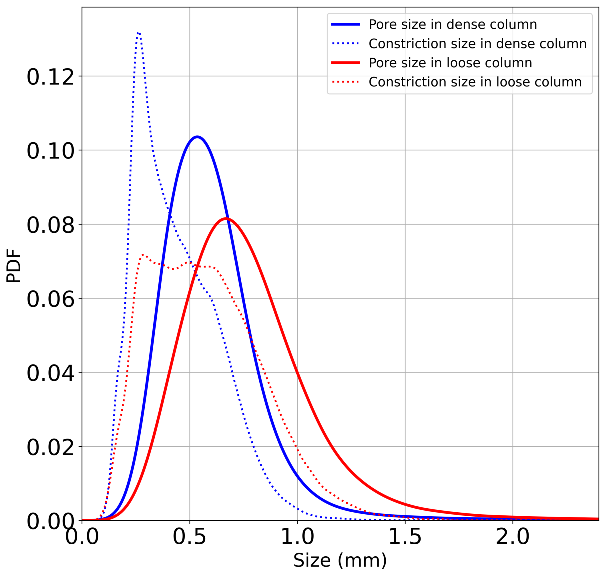

Fig. 7: Probability distribution of pore and constriction size in the loose (red) and dense (blue) columns based on Delaunay triangulation.

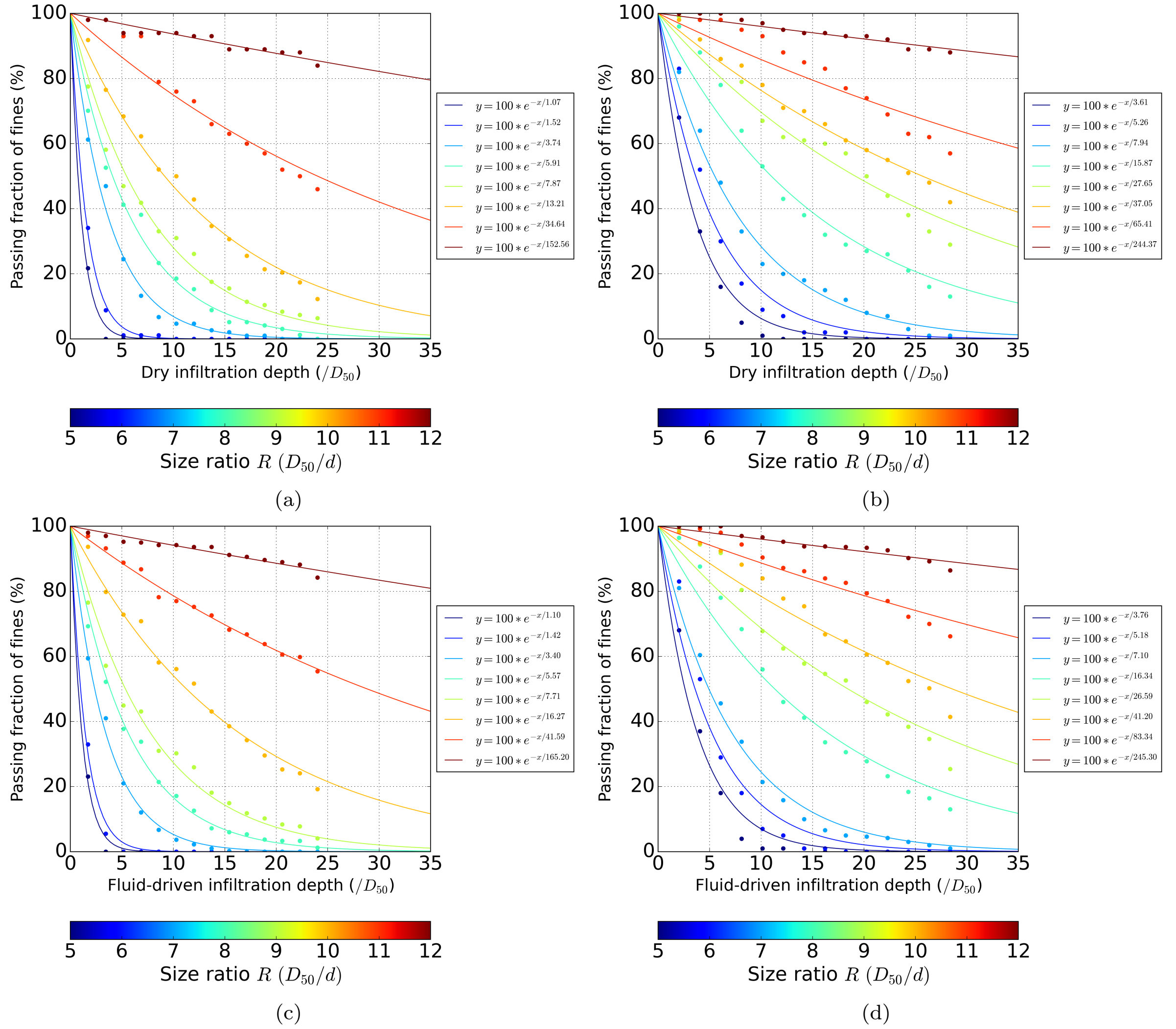

Fig. 8: Fitted exponential decay curves based on fine passing fraction using $y = 100 * e^{(-z/L_0)}$: (a), (b) dry infiltration in dense and loose columns; (c), (d) fluid-driven infiltration in dense and loose columns.

7, suggesting that in the surface clogging regime, packing density or void ratio e of the column has little effect on L_0. Then, in the deep infiltration regime, L_0 increases sharply but to distinct extents depending on the density of the base soil. For instance, when R is 8, 9, and 10, L_0 is three times larger in the loose column compared to the dense one. In the end, for R greater than 10, the percolation depth of L_0 increases dramatically, reflecting a transition from deep bed filtration to unimpeded percolation. In the context of soil erosion by seepage flow, this behavior highlights the high susceptibility of the fine fraction.

Another observation is the slight but noticeable increase in L_0 in fluid-driven infiltration cases compared to dry ones in both loose and dense columns. The difference is initially negligible at the beginning when R is lower than 9. Previous studies [19, 2] suggested that the hydraulic channels might drive the fine particles to explore more lateral paths compared to dry conditions. In this study, when R is smaller than 9, most fine sands are retained at shallow depth due to void geometry, thus the hydraulic force plays a limited role in boosting penetration. Whereas, as the fine sands are getting smaller, the fluid-driven lateral movement becomes prominent (see detailed analysis in subsection 3.5). According to Figure 9, L_0 increases from $34D_{50}$ and $65D_{50}$ to $41D_{50}$ and $83D_{50}$ for R equal to 11 in dense and loose column respectively. This supports the assumption from existing literature that hydraulic forces may favor the infiltration of fine sands as indicated by the augmentation of L_0 in Figure 9. It should be highlighted here that such a feature could only be observed under a pore-scale fluid-grain coupling scheme (PFV or other resolved CFD methods), whereas the conventional unresolved CFD-DEM, relying on averaged fluid friction under coarse fluid mesh, is not adapted to capture these fine-scale hydraulic effects.

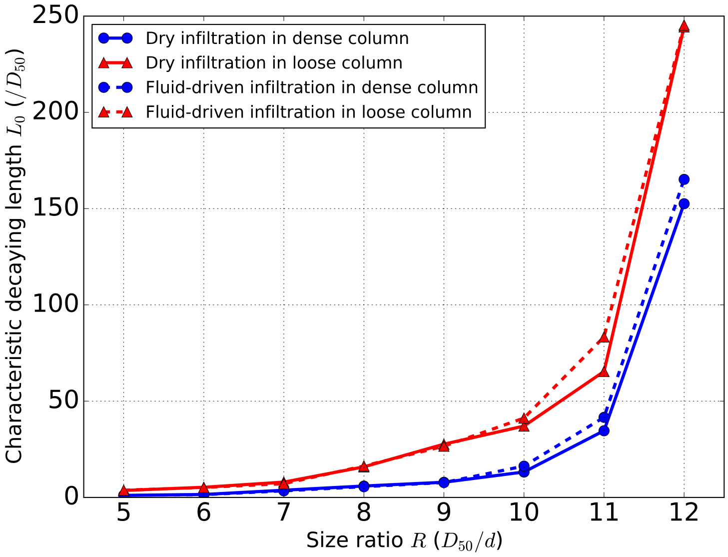

Fig. 9: Comparison of characteristic decaying length L_0 in all cases.

3.3 Microstructurally-based probabilistic model

In this section, a simple probabilistic model is proposed based on the fine particle diameter and pore-constriction size statistics [24]. This model aims at understanding and predicting the fine particle retention distribution represented by the previous decaying length L_0. The model is based on the following assumptions: (1) The geometry or pore network within the base soil is homogeneous; (2) The probability of fine sands clogging is determined by the proportion of constrictions smaller than fine sand diameter; (3) Constrictions are equally spaced from one another; (4) Only downward fine particles displacements are considered with no lateral propagation.

Consequently, the build-up of this model is as follows:

1. Firstly, given the statistics of pore-constriction size shown in Figure 7, the probability for a fine particle of diameter d to pass a constriction is derived as the percentage of constrictions larger than d ($d_{cons} > d$) among all the constrictions. This probability is denoted as P_d. Figure 10(a) plots the PDF of D_{50}/d_{cons} in loose and dense columns with the dotted vertical lines representing different diameters of fine particles successively implemented. The computed results of P_d are given in Figure 10(b). The results show that P_d depends on the sample density for R values up to 12 as considered in this study.
2. Then, based on a homogeneous assumption of pore-constriction size in the soil sample, it is assumed that fine particles always move between pores of fixed size that equals to the median value of pore size $D_{p_{50}}$. Here, $D_{p_{50}}$ is equal to $0.334D_{50}$ and $0.424D_{50}$ for dense and loose sample respectively (see Figure 7). Each time a fine particle passes through a constriction, its local penetration depth is incremented by an elementary drop path Δz. This mean distance between two successive constrictions can be calculated using an ideal granular configuration of two neighboring tetrahedrons formed by five closely contacting grains as shown in Figure 10(c). In this configuration, Δz is correlated to D_{pore} by a multiplicative ratio λ defined by $\frac{\Delta z}{D_{pore}} = \frac{\sqrt{6}}{3(\sqrt{6}-2)}$. Consequently, Δz is equals to $0.60D_{50}$ and $0.77D_{50}$ in dense and loose column respectively. Interestingly, this physics-based ratio has been observed in another similar numerical work [18], where the averaged Δz between two passable throats is found very consistent ranging from $0.65D_{50}$ to $0.72D_{50}$ across varied packing densities with limited change in R.
3. Finally, the probability for a fine grain to be stopped at depth z is $P_d^{z/\lambda D_{p_{50}}}$ since it has to cross a number of constrictions equal to $z/\lambda D_{p_{50}}$. The exponential decay of the fine retention PDF can be recovered based on P_d and $D_{p_{50}}$ as we can define L_0 as:

$$L_0 = \frac{-1}{(3-\sqrt{6})} D_{p_{50}} / \ln(P_d) \tag{7}$$

Figure 10(d) compares the predicted values of L_0 for each given size of injected fine sands with the fitting results of the fine grain retention PDFs from the simulation. Interestingly, this simple probabilistic model is found to predict quite well the characteristic length L_0, showing a linear trend for $\log(L_0)$ versus R in both dense and loose columns. This consistency between the model prediction and the simulation validates the idea that the average probability P_d of fine particles passing through constrictions in soil with

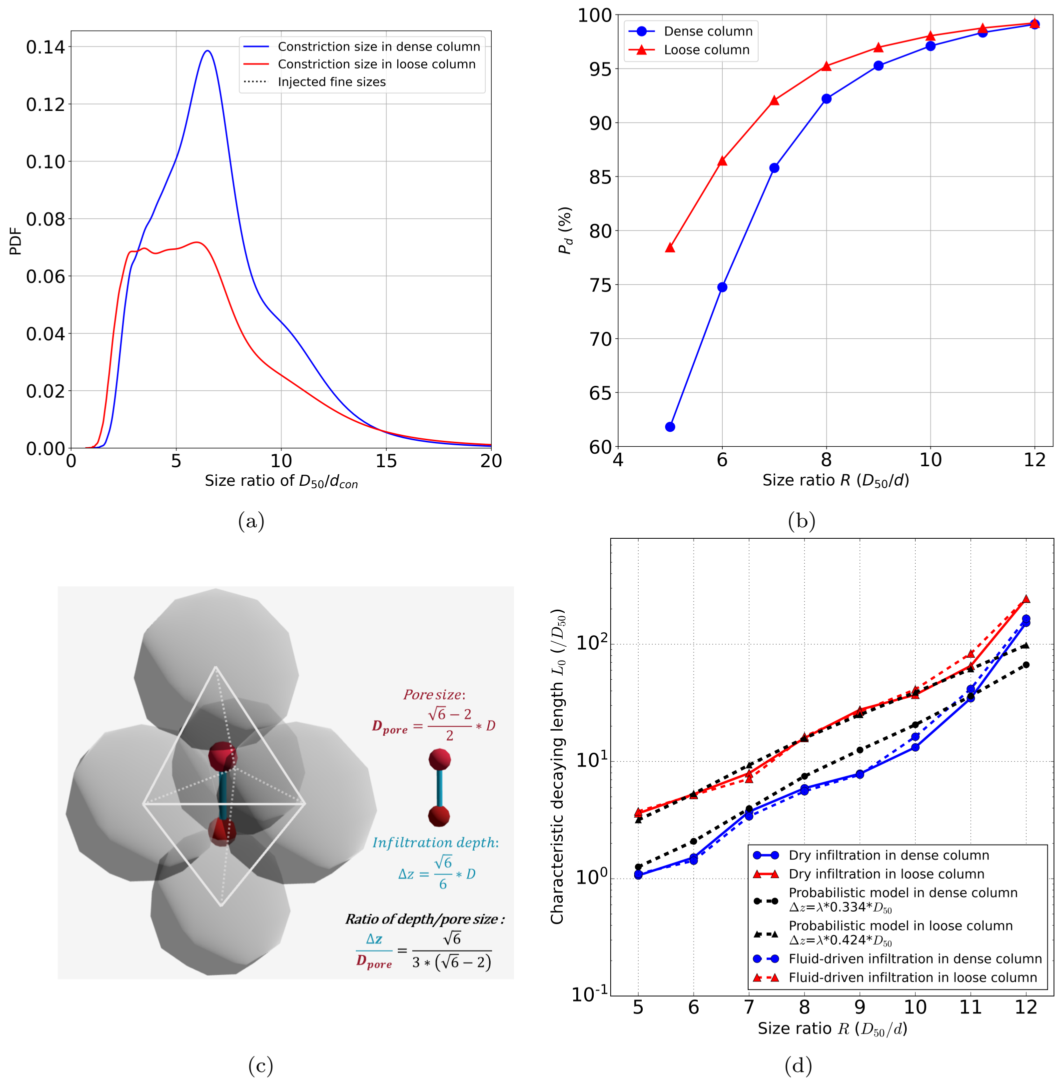

Fig. 10: Build-up of probabilistic model predicting L_0: (a) PDF of D_{50}/d_{con} in loose and dense columns (with d_{con} being the constriction diameter); (b) computed passing probability P_d in dense and loose column for each given fine diameter d; (c) schematic of the ideal granular configuration of two neighboring tetrahedrons made of five closely contacting grains and derivation of Δz from D_{pore}; (d) L_0 as a function of size ratio R obtained from previous simulations and probabilistic approach.

a homogeneous pore-constriction network captures the key physics governing their infiltration. Furthermore, the linear trend observed between $\log(L_0)$ and R suggests a systematic relationship between the size ratio and the characteristic infiltration depth, highlighting the importance of considering PSD when predicting fine particle retention in the base soil.

3.4 Averaged penetration velocity

When fine particles infiltrate into granular material, they are likely to reach a mean steady percolation velocity resulting from the interplay between driving forces (gravity or fluid) and collision with coarse grains [31]. To evaluate this mean velocity V we calculate the total vertical displacement of each particle divided by its total time interval from its entry into the static bed until either being clogged or reaching the bottom of the column. In Figure 11(a), the values of V are plotted against size ratio R being normalized by $\sqrt{2gD_{50}}/2$. This normalization accounts for the averaged velocity of a grain in free fall over a distance of D_{50} driven by gravity [12]. These values are compared with previous experimental and numerical data [25, 18, 7], revealing a positive correlation of dimensionless velocity with R and a negative correlation with ϕ. This last result can be attributed to the fact that denser packing (higher value of ϕ) or larger fine size increases the probability of particle bouncing and thus disturbs the free falling of fine sands.

Since we considered both the densest and loosest limits, the numerical result represents the whole range of infiltration velocity magnitudes whatever the packing density for each given R. Consistently with previous works, we can conclude that the dimensionless velocity seems to smoothly increase from surface clogging to percolating regime since no sharp turning point is observed.

To further quantify the influences of ϕ and R, an approximate scaling can be proposed when multiplying the dimensionless velocity by $\phi/\sqrt{R}$. As previously introduced by [17], this scaling in Figure 11(b) almost brings the data together, around a roughly constant value of approximately 0.075 regardless of R and ϕ. Even though the physical meaning behind this scaling remains unclear according to [18], this strategy is promising for estimating the penetration velocity in future research. Based on the mean infiltration depth L_0 and velocity V, a characteristic duration $T_0 = L_0/V$ is calculated in Figure 11(c). Interestingly, T_0 follows a linear exponential increasing trend with R as L_0 in Figure 9, meaning that T_0 is mostly governed by the magnitude of L_0, despite of higher infiltration velocity for the finer injected particles.

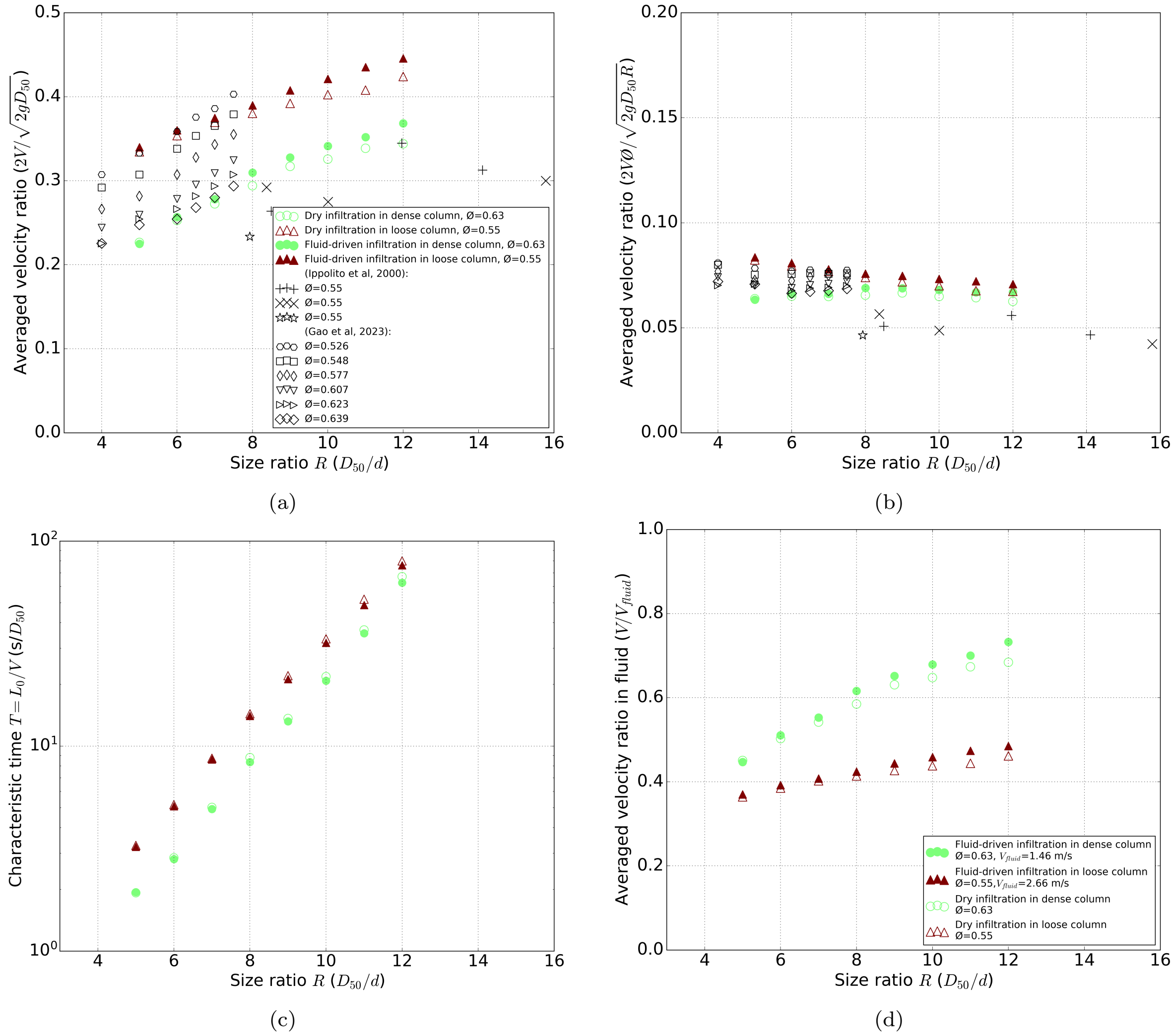

Fig. 11: Dimensionless mean percolation velocity for various R with comparison to existing numerical [18] and experimental [25] data: (a) normalized percolation velocity $2V/\sqrt{2gD_{50}}$; (b) proposed scaling the normalized percolation velocity by solid fraction and size ratio $2V\phi/\sqrt{2gD_{50}R}$ to achieve a constant level; (c) characteristic infiltration time T_0 using L_0 divided by averaged velocity V; (d) normalized averaged velocity V scaled by the mean fluid velocity V_{fluid} based on PFV calculation.

Considering the fluid-driven infiltration simulations presented in Figure 11(d), the averaged fine grain percolation velocity is no longer normalized by a free fall velocity but alternatively by the average flow velocity computed in the PFV method since the relative velocity between the liquid flow and a mobile particle ($|v_p - v_{fluid}|$) now drives the infiltration process. Here, the averaged fluid velocity V_{fluid} is calculated based on Darcy's flow relation in porous media given by $v_{fluid} = Q/(S(1-\phi))$, where Q is the volume flow rate and S is the cross-section perpendicular to flowing direction. V_{fluid} is 1.46 m/s and 2.66 m/s in dense and loose column respectively. From Figure 11(d), an increasing relative gap can be observed for R under different densities with a range of 0.36 to 0.5 for the loose column, and a higher ratio from 0.45 to 0.7 for the dense column. This indicates that the relative velocity between the fluid flow and fine particles plays a crucial role in driving the infiltration process, with denser soil samples experiencing higher driving forces due to the increased fluid velocities.

3.5 Lateral dispersion

During infiltration, the injected particles also move laterally, due to the pore space tortuosity and random collisions with the coarse grains. The fine particle's lateral displacement, denoted as r, is introduced as the deviation from its initial position on the horizontal plane. The classical diffusion-based theory suggests a relationship between lateral mean square displacement and time: $\langle r^2 \rangle = Dt$, where D is the lateral dispersion coefficient and t is the duration spent in the porous bed. Previously the penetration depth z of fine particles can be obtained by the mean velocity Vt. Therefore in Figure 12 the dimensionless mean square lateral displacement $\langle r^2 \rangle / D_{50}^2$ is plotted against the dimensionless infiltration depth z/D_{50}. The high degree of linearity observed corresponds well to the diffusion-based theory by $\langle r^2 \rangle = kz$, where k equals $D/(VD_{50})$. It suggests that lateral particle movement during infiltration can be effectively described by diffusion processes, with k providing a measure of the relationship between lateral dispersion, mean velocity, and particle size.

In dry infiltration, the dimensionless mean square lateral dispersion curves of $\langle r^2 \rangle / D_{50}^2$ versus z/D_{50} are shown in Figure 12(a) by dotted and solid lines for dense and loose columns respectively. The slope k of the curve is found to increase with R but within distinct ranges depending on whether the column is loose or dense. The lowest lateral dispersion coefficients and the smallest penetration depths are obtained in the dense case. In fluid-driven cases plotted in Figure 12(b), the lateral dispersion is shown to be somewhat increased compared to dry infiltration. The average values of the dimensionless lateral dispersion coefficient k are given for all curves in Figure 12(c). Indeed, the fluid-driven cases enhance the lateral coefficient compared to dry infiltration, particularly in the loose column. The reason is that in fluid-driven infiltration, the preferential path follows the maximal inter-pore hydraulic gradient, while in dry infiltration, the preferential path is more likely to be parallel with gravitational force. Consequently, more laterally oriented preferential paths are explored in the hydraulic-oriented infiltration compared to gravity-driven conditions.

The simulated results in dry conditions are compared here with a set of dry infiltration experiments from [25]. These experiments provide a reference range of k of gravity-driven infiltration behavior of stainless steel particles into a loose granular column (ϕ=0.55, same as the loose sand column in this work) considering R values of 8.61 and 14.2. The experimental lateral displacement data are set to zero to avoid the influence of arbitrary bouncing of the fine particles above the column since they are dropped from a certain altitude, possibly leading to a non-zero $\langle r^2 \rangle$ when infiltration depth is zero according to [25]. The values of k in [25] are plotted in Figure 12(c), showing that they are slightly higher than the numerical results in the loose column but are of the same order of magnitude. This difference is probably due to the restitution coefficient of stainless steel particles, which is typically higher than 0.8 according to previous studies [25, 38], while it is set to 0.3 in this numerical work. Although the effect of the restitution coefficient on lateral dispersion is beyond the scope of this work, this comparison indicates that experimental measurements and numerical calculations can achieve a level of alignment from the lateral dispersion aspect.

Based on the linearity of $\langle r^2 \rangle$ with z and the collapse of the dimensionless mean velocity multiplied by $\phi/\sqrt{R}$ to 0.075, the classic diffusion-based theory of $\langle r^2 \rangle = Dt$ could be rewritten as follows:

$$\langle r^2 \rangle = \frac{0.075\sqrt{gD_{50}R/2}}{\phi} D_{50} k t \tag{8}$$

in which the magnitude of k ranges from 0.2 to 0.4 in the loose column and from 0.07 to 0.27 in the dense one based on Figure 12(c), meaning that a further dependency with R is still missing to reach a complete scaling. Equation 8 could provide an estimation of the lateral dispersion coefficient D of fine infiltration in coarse-grain media based on its packing density ϕ and size ratio R.

4 Conclusion and outlook

The fine injection into the eroded dam body is primarily investigated numerically via the coupled PFV-DEM approach. The infiltration and clogging of injected fine particles into the soil column are simulated considering a wide range of particle size ratio R, column packing solid fraction ϕ, and gravity or fluid-driven condition. The transfers of three distinct fine clogging regimes are identified, shedding light on the

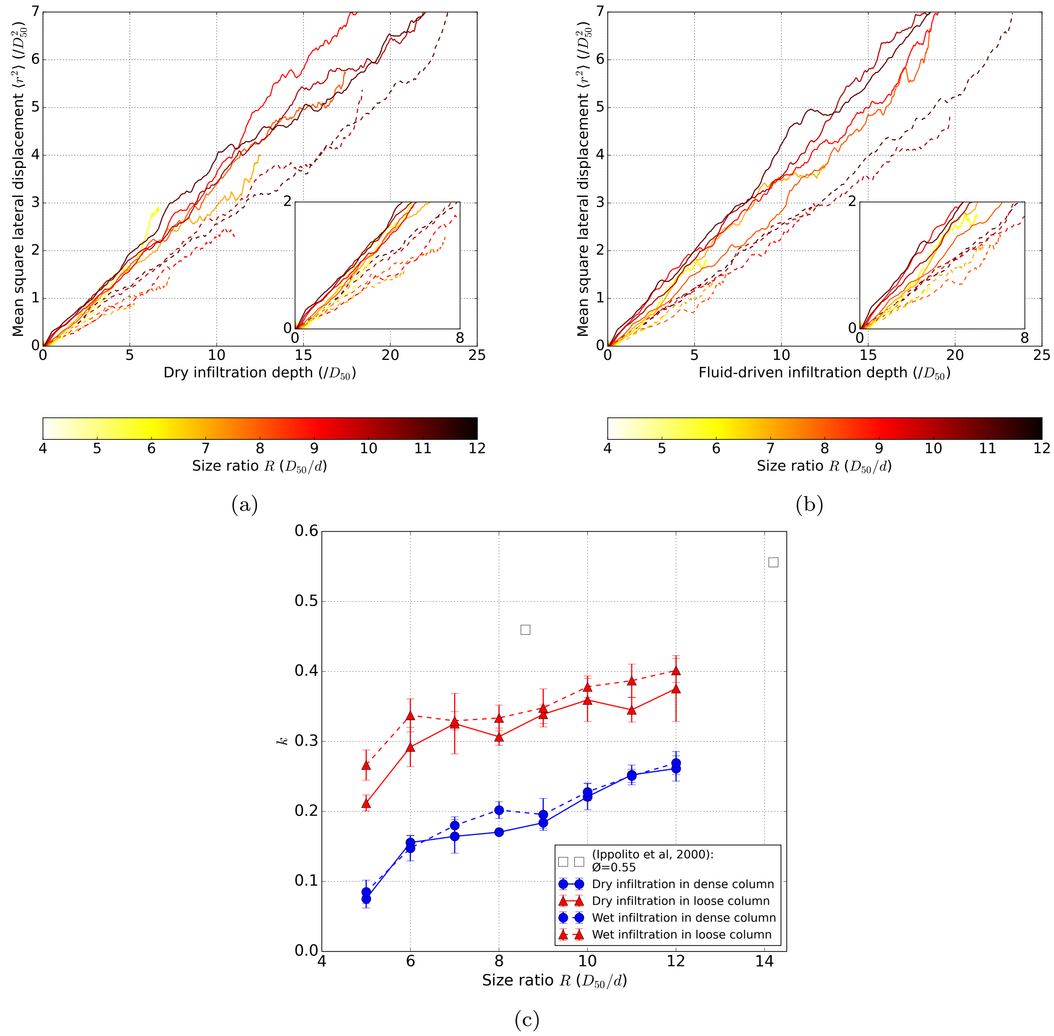

Fig. 12: Lateral dispersion curves: mean square lateral displacement $\langle r^2 \rangle$ of injected fine sands along vertical penetration depth: (a) Dry infiltration; (b) Fluid-driven infiltration; (c) Averaged slope k values of all curves in comparison with dry infiltration experiments from [25].

complex interplay between particle size, soil packing density, and infiltration dynamics. The fine retention distribution, averaged penetration velocity and lateral dispersion are thoroughly analyzed to understand the underlying mechanisms governing fine particle transport in porous media. The main conclusions are as follows:

- The characteristic decaying length L_0 of fine retention increases exponentially with R, but at a lower rate in the denser soil column than in the loose column, underlying the effect of particle size and density; and fluid-driven infiltration has an enhancing but rather limited effect on fine infiltration depth.
- Taking into account the statistical distribution of pores and constrictions, a probabilistic model is proposed to interpret L_0 in terms of mean traveling distance through pores and constrictions. It is demonstrated that our model, despite its simplicity, can provide encouraging estimation on fine particle retention considering multiple factors such as soil density and size ratio R.
- No sharp transitions of averaged penetration velocity are found for different clogging regimes with increasing R in both gravity or fluid-driven conditions. When scaled properly, the averaged penetration velocity of fine sands during infiltration would converge to a constant value using the normalization strategy of $\phi/\sqrt{R}$.
- The square lateral displacement increases linearly with penetration depth and correlates positively with R and negatively with packing density, with an alignment with experimental measurements from [25]. Moreover, laterally oriented preferential paths are explored in the hydraulic-oriented infiltration compared to gravity-driven conditions. Finally, the lateral dispersion coefficient D could be estimated using $r^2 = \frac{0.075\sqrt{gD_{50}R/2}}{\phi}D_{50}kt$.

The numerical results mentioned above suggest that when injecting fine particles of fixed size into an eroded dam body, the method is effective within a certain remediation distance (passing fraction at averaged infiltration depth) varying with infiltration condition, size ratio R, and base soil solid fraction ϕ. Also, the remediated area in the perpendicular direction should be carefully examined, since it can be limited under relatively high soil compaction. Therefore, the effectiveness of the injection remediation is probably more suited for relatively loosely compacted granular material. It is worth noting that a comparison of our model with experimental tests is currently in progress and will be presented shortly.

Several perspectives for future research in the field of injection remediation for dam erosion control can be proposed as follows: one is the optimization of the PSD and concentration of injected sand suspension for achieving more efficient retention by considering poly-dispersity and the collective effect of clogging by bridging or straining. For this purpose, the zero-friction condition of fine sands applied in this study must be relaxed, so that the model will be no longer limited to fine capture and retention only due to size exclusion. On the contrary, it could include multi-particle mechanisms as clogging or local arching and thus be considered as the upper bound of infiltration distance. Second, the derived probabilistic model has the potential for an extended application to predict the fine retention distribution. By using the pore-constriction statistics obtained from scanning technologies such as Computed Tomography (CT) or Scanning Electron Microscope (SEM), or from numerical samples via DEM, the model could be further refined and applied to various scenarios. Future work will also focus on investigating the enhanced mechanical strength and stability of eroded soil induced by fine injection in deep infiltration conditions, according to the second-order work criterion [49, 52].

5 Acknowledgments

This study was financially supported by the China Scholarship Council (CSC) (No. 20220700024). For Open Access, a CC-BY public copyright license has been applied by the authors to the present document and will be applied to all subsequent versions up to the Author Accepted Manuscript arising from this submission.

6 Declaration of interests

None.

References

1. Abdallah, A., Vincens, E., Magoariec, H., 2022. Dry and wet filtration in granular filters: a dem modeling, in: 25e Congrès Français de Mécanique, Nantes.
2. Abdallah, A., Vincens, E., Magoariec, H., Picault, C., 2024. Dem filtration modelling for granular materials: Comparative analysis of dry and wet approaches. International Journal for Numerical and Analytical Methods in Geomechanics 48, 870–886. doi:https://doi.org/10.1002/nag.3666.
3. Bonelli, S., 2012. Erosion of geomaterials. John Wiley & Sons.
4. Bonelli, S., 2013. Erosion in geomechanics applied to dams and levees. John Wiley & Sons.
5. Bridgwater, J., 1976. Fundamental powder mixing mechanism. Powder Technology 15, 215–236.
6. Bridgwater, J., Ingram, N., 1971. Rate of spontaneous inter-particle percolation. Transactions of the Institute of Chemical Engineers 49, 163–169.
7. Bridgwater, J., Sharpe, N., Stocker, D., 1969. Particle mixing by percolation. Transactions of the Institute of Chemical Engineers 47, T114–T119.
8. Caulk, R.A., Catalano, E., Chareyre, B., 2020. Accelerating yade's poromechanical coupling with matrix factorization reuse, parallel task management, and gpu computing. Computer Physics Communications 248, 106991. doi:https://doi.org/10.1016/j.cpc.2019.106991.
9. Chareyre, B., Cortis, A., Catalano, E., Barthélemy, E., 2012. Pore-scale modeling of viscous flow and induced forces in dense sphere packings. Transport in porous media 94, 595–615. doi:10.1007/s11242-011-9915-6.
10. Chen, F., Jiang, S., Xiong, H., Yin, Z.Y., Chen, X., 2023a. Micro pore analysis of suffusion in filter layer using tri-layer CFD–DEM model. Computers and Geotechnics 156, 105303. doi:10.1016/j.compgeo.2023.105303. hal-04300945.
11. Chen, F., Xiong, H., Wang, X., et al., 2023b. Transmission effect of eroded particles in suffusion using the cfd-dem coupling method. Acta Geotechnica 18, 335–354. doi:10.1007/s11440-022-01568-8.
12. Cooke, M., Bridgwater, J., Scott, A., 1978. Interparticle percolation: lateral and axial diffusion coefficients. Powder Technology 21, 183–193. doi:https://doi.org/10.1016/0032-5910(78)80088-6.

13. Cundall, P.A., Strack, O.D.L., 1979. A discrete numerical model for granular assemblies. Géotechnique 29, 47–65. doi:10.1680/geot.1979.29.1.47.
14. Dudill, A., Frey, P., Church, M., 2017. Infiltration of fine sediment into a coarse mobile bed: a phenomenological study. Earth Surface Processes and Landforms 42, 1171–1185. doi:https://doi.org/10.1002/esp.4080.
15. Frey, P., Church, M., 2011. Bedload: a granular phenomenon. Earth Surface Processes and Landforms 36, 58–69. doi:https://doi.org/10.1002/esp.2103.
16. Frostick, L.E., Lucas, P.M., Reid, I., 1984. The infiltration of fine matrices into coarse-grained alluvial sediments and its implications for stratigraphical interpretation. Journal of the Geological Society 141, 955–965. doi:10.1144/gsjgs.141.6.0955.
17. Gao, S., Ottino, J.M., Umbanhowar, P.B., Lueptow, R.M., 2023. Percolation of a fine particle in static granular beds. Phys. Rev. E 107, 014903.
18. Gao, Z., Tang, Y., Chen, Y., Wang, X., 2024. Mechanism of the post-suffusion mechanical response of gap-graded soils from the perspective of force-chain evolution. Computers and Geotechnics 165, 105946.
19. Ghidaglia, C., de Arcangelis, L., Hinch, J., Guazzelli, E., 1996a. Hydrodynamic interactions in deep bed filtration. Physics of Fluids 8, 6–14.
20. Ghidaglia, C., de Arcangelis, L., Hinch, J., Guazzelli, E., 1996b. Transition in particle capture in deep bed filtration. Phys. Rev. E 53, R3028–R3031. doi:10.1103/PhysRevE.53.R3028.
21. Gibson, S., Heath, R., Abraham, D., Schoellhamer, D., 2011. Visualization and analysis of temporal trends of sand infiltration into a gravel bed. Water Resources Research 47. doi:https://doi.org/10.1029/2011WR010486.
22. Hadda, N., Nicot, F., Bourrier, F., Sibille, L., Radjai, F., Darve, F., 2013. Micromechanical analysis of second order work in granular media. Granular matter 15, 221–235.
23. Indraratna, B., Raut, A.K., Khabbaz, H., 2007a. Constriction-based retention criterion for granular filter design. Journal of Geotechnical and Geoenvironmental Engineering 133, 266–276. doi:10.1061/(ASCE)1090-0241(2007)133:3(266).
24. Indraratna, B., Raut, A.K., Khabbaz, H., 2007b. Constriction-based retention criterion for granular filter design. Journal of Geotechnical and Geoenvironmental Engineering 133, 266–276. doi:10.1061/(ASCE)1090-0241(2007)133:3(266).
25. Ippolito, I., Samson, L., Bourlès, S., Hulin, J.P., 2000. Diffusion of a single particle in a 3d random packing of spheres. The European Physical Journal E 3, 227–236. doi:10.1007/PL00013679.
26. Jaeger, H.M., Nagel, S.R., Behringer, R.P., 1996. Granular solids, liquids, and gases. Rev. Mod. Phys. 68, 1259–1273. doi:10.1103/RevModPhys.68.1259.
27. Kenney, T., Lau, D., 1985. Internal stability of granular filters. Canadian Geotechnical Journal 22, 215–225. doi:10.1139/t85-029.
28. Kenney, T.C., Chahal, R., Chiu, E., Ofoegbu, G.I., Omange, G.N., Ume, C.A., 1985. Controlling constriction sizes of granular filters. Canadian Geotechnical Journal 22, 32–43. doi:10.1139/t85-005.
29. Kerimov, A., Mavko, G., Mukerji, T., Al Ibrahim, M.A., 2018. Mechanical trapping of particles in granular media. Phys. Rev. E 97, 022907. doi:10.1103/PhysRevE.97.022907.
30. King, J., Loveday, I., Schuster, R.L., 1989. The 1985 bairaman landslide dam and resulting debris flow, papua new guinea. Quarterly Journal of Engineering Geology and Hydrogeology 22, 257–270.
31. Li, M., Chen, H., Li, X., Liu, L., Lin, J., 2022. Permeability of granular media considering the effect of grain composition on tortuosity. International Journal of Engineering Science 174, 103658. doi:https://doi.org/10.1016/j.ijengsci.2022.103658.
32. Li, S., Russell, A.R., Muir Wood, D., 2020. Influence of particle-size distribution homogeneity on shearing of soils subjected to internal erosion. Canadian Geotechnical Journal 57, 1684–1694.
33. Li, S., Russell, A.R., Muir Wood, D., 2024. Internal erosion of a gap-graded soil and influences on the critical state. Acta Geotechnica 19, 5363–5381.
34. Lominé, F., Oger, L., 2009. Dispersion of particles by spontaneous interparticle percolation through unconsolidated porous media. Phys. Rev. E 79, 051307. doi:10.1103/PhysRevE.79.051307.
35. Lominé, F., Oger, L., 2010. Transit time during the interparticle percolation process. Phys. Rev. E 82, 041301. doi:10.1103/PhysRevE.82.041301.
36. Luo, Y., Luo, B., Xiao, M., 2020. Effect of deviator stress on the initiation of suffusion. Acta Geotechnica 15, 1607–1617. doi:10.1007/s11440-019-00859-x.
37. Ma, Q., Wautier, A., Nicot, F., 2022. Mesoscale investigation of fine grain contribution to contact stress in granular materials. Journal of Engineering Mechanics 148, 04022005. doi:10.1061/(ASCE)EM.1943-7889.0002078.
38. Masliyah, J., Bridgwater, J., 1974. Particle percolation: a numerical study. Trans. Instn Chem. Engrs 52, 31–42.

39. Muzzio, F., Robinson, P., Wightman, C., Dean Brone, B., 1997. Sampling practices in powder blending. International Journal of Pharmaceutics 155, 153–178. doi:10.1016/S0378-5173(97)04865-5.
40. Nguyen, C.D., Benahmed, N., Andò, E., et al., 2019. Experimental investigation of microstructural changes in soils eroded by suffusion using x-ray tomography. Acta Geotechnica 14, 749–765. doi:10.1007/s11440-019-00787-w.
41. Roozbahani, M.M., Graham-Brady, L., Frost, J.D., 2014. Mechanical trapping of fine particles in a medium of mono-sized randomly packed spheres. International Journal for Numerical and Analytical Methods in Geomechanics 38, 1776–1791. doi:https://doi.org/10.1002/nag.2276.
42. Sakthivadivel, R., Einstein, H.A., 1970. Clogging of porous column of spheres by sediment. Journal of the Hydraulics Division 96, 461–472. doi:10.1061/JYCEAJ.0002332.
43. Savage, S.B., Lun, C.K.K., 1988. Particle size segregation in inclined chute flow of dry cohesionless granular solids. Journal of Fluid Mechanics 189, 311–335. doi:10.1017/S002211208800103X.
44. Seed, H.B., Duncan, J.M., 1987. The failure of teton dam. Engineering Geology 24, 173–205.
45. Shire, T., O'Sullivan, C., 2016. Constriction size distributions of granular filters: a numerical study. Géotechnique 66, 826–839. doi:10.1680/jgeot.15.P.215.
46. Sibille, L., Marot, D., Sail, Y., 2015. A description of internal erosion by suffusion and induced settlements on cohesionless granular matter. Acta Geotechnica 10, 735–748. doi:10.1007/s11440-015-0388-6.
47. Thevanayagam, S., Shenthan, T., Mohan, S., Liang, J., 2002. Undrained fragility of clean sands, silty sands, and sandy silts. Journal of Geotechnical and Geoenvironmental Engineering 128, 849–859. doi:10.1061/(ASCE)1090-0241(2002)128:10(849).
48. Vincens, E., Witt, K.J., Homberg, U., 2015. Approaches to determine the constriction size distribution for understanding filtration phenomena in granular materials. Acta Geotechnica 10, 291–303. doi:10.1007/s11440-014-0308-1.
49. Wang, T., Wautier, A., Liu, S., Nicot, F., 2022. How fines content affects granular plasticity of underfilled binary mixtures. Acta Geotechnica 17, 2449–2463. doi:10.1007/s11440-021-01430-3.
50. Wautier, A., Bonelli, S., Nicot, F., 2017. Scale separation between grain detachment and grain transport in granular media subjected to an internal flow. Granular Matter 19, 22. doi:10.1007/s10035-017-0706-9.
51. Wautier, A., Bonelli, S., Nicot, F., 2019a. Dem investigations of internal erosion: Grain transport in the light of micromechanics. International Journal for Numerical and Analytical Methods in Geomechanics 43, 339–352. doi:https://doi.org/10.1002/nag.2866.
52. Wautier, A., Bonelli, S., Nicot, F., 2019b. Rattlers' contribution to granular plasticity and mechanical stability. International Journal of Plasticity 112, 172–193. doi:https://doi.org/10.1016/j.ijplas.2018.08.012.
53. Williams, J., 1968. The mixing of dry powders. Powder Technology 2, 13–20. doi:https://doi.org/10.1016/0032-5910(68)80028-2.